Open access • Proceedings Article • DOI:10.14264/618AC78

Heat Transfer Investigation on Under-expanded Supersonic Impinging Jets by Large Eddy Simulation — Source link

Minghang Li, Richard D. Sandberg, Julio Soria, Andrew Ooi

Published on: 11 Dec 2020

Topics: Large eddy simulation, Supersonic speed and Heat transfer

22nd Australasian Fluid Mechanics Conference AFMC2020
Brisbane, Australia, 7–10 December 2020
https://doi.org/10.14264/618ac78

Heat Transfer Investigation on Under-expanded Supersonic Impinging Jets by Large Eddy Simulation

M. Li[1], R. D. Sandberg[1], J.Soria[2] and A. Ooi[1]

[1] Department of Mechanical Engineering
University of Melbourne, Victoria 3010, Australia

[2] Laboratory for Turbulence Research in Aerospace & Combustion
Department of Mechanical and Aerospace Engineering
Monash University, Victoria 3800, Australia

Abstract

Under-expanded jets impinging on an adiabatic and a heated wall have been numerically studied by wall-resolved compressible Large Eddy Simulation (LES). The jets are characterised with an infinite lip and a Reynolds number of 6×10^4 based on an ideally-expanded jet velocity and a nozzle diameter D. The distance between the nozzle and the plate is $5D$. A nozzle pressure ratio (NPR) of 3.4 is considered to investigate how the compressibility effect and shock waves affect the thermal behaviours close to the wall. A barycentric map is then utilised to further investigate the near-wall turbulence. It is found that the anisotropic turbulence exhibits one-directional fluctuations at the location where a secondary minimum of Nusselt number occurs. It is proposed that this behaviour could be explained by the generation of shocklets in the wall jet, leading to the reduced heat removal capability.

Keywords
Heat transfer; Impinging jet; Supersonic.

Introduction

Heat transfer of impinging jets has been investigated over many decades for its good efficiency of cooling or heating a surface, such as the cooling of turbine blades and the heating produced by the short take off and vertical landing aircraft (STVOL). A recent summary [1] comprehensively reported on the jet impingement heat transfer for subsonic jets investigated experimentally and numerically. It highlighted that the efficiency of transferring energy mainly depends on the jet Reynolds number, the jet-plate distance and the nozzle geometry. However the above three parameters are not sufficient to characterise the supersonic impinging jets due to the presence of high compressibility and the shock structures. Although there are extensive studies on under-expanded impinging jets, most of the research focused on the flow physics only [2–4] and only little attention was paid to the heat transfer. Based on the current available data, an experimental observation [5] found that the shock waves would strongly affect the heat transfer performance within limited jet-place distances. At the same Reynolds number and a relatively short jet-plate spacing, increasing the stagnation pressure from subsonic to supersonic jet conditions would shift the maximum Nusselt number away from the stagnation point, whilst a secondary minimum and maximum Nusselt number could be found on the wall. In addition, with an appropriate stagnation pressure, the heat transfer rate would be doubled over that of the subsonic jet impingement. This indicates that the compressibility effect and the strong shock waves play an important role in the heat transfer efficiency. It is thus expected that the mechanism responsible for the formation of dip and peak in Nusselt numbers is different from that of subsonic jet impingement.

This paper presents wall-resolved Large Eddy Simulation (LES) of two under-expanded supersonic impinging jets with an adiabatic and a heated wall boundary condition. The objective of this paper is to provide insights into the generation of the secondary minimum and maximum of the Nusselt numbers under the current supersonic condition and propose an appropriate explanation for this phenomenon.

Numerical Setup

The simulations solve the full, non-dimensionlised, filtered compressible Navier-Stokes equations in cylindrical coordinates using a high-fidelity in-house code (HiPSTAR) [6]. A standard fourth-order finite differencing scheme is applied to both the streamwise and radial directions, whilst a Fourier spectral method is utilised in the azimuthal direction. The temporal integration is performed by an explicit fourth-order Runge-Kutta scheme. For the LES, the Wall-Adapting-Local-Eddy (WALE) model [7] with the standard coefficient of 0.325 is used for the contribution of subgrid scales due to its straightforward implementation and the proper recovery of the near-wall scaling. The diffusivity of the sub-grid scales is solved by assuming a constant turbulent Prandtl number (Pr_t) of 0.9. The code has recently been validated by [8] for subsonic impinging jets.

The computational domain consists of 5 blocks including a short pipe (*Block 1*), a main-jet region (*Block 2*), a shear-layer region (*Block 3*), a near-field region (*Block 4*) and a far-field region (*Block 5*). A schematic of the configuration is shown in figure 1. At the pipe inlet of *Block 1*, a hyperbolic-tangent function [9] is applied for the inlet axial velocity. The density and temperature at the inlet are uniform following the choked condition except close to the pipe wall. All the walls have the no-slip and adiabatic conditions, except for the heated case for which a constant temperature is prescribed on the impingement wall. Since the contraction ratio of the experimental nozzle is high enough to annihilate the incoming turbulence, no artificial turbulence is generated inside the pipe which allows us a direct comparison with the experimental data [11]. In the axial direction (x), the short pipe (*Block 1*) is discretised with a uniform grid size of $\Delta x/D = 0.001$. For the rest of the blocks, the axial mesh spacing gradually increases to $\Delta x/D = 0.02$ from $x/D = 0$ to $x/D = 1.45$ with a stretching ratio of around 1%. The grid size is kept uniform with $\Delta x/D = 0.02$ up to $x/D = 3.57$ and gradually decreases to $\Delta x/D = 0.0002$ with a stretching ratio of less than 1% close to the impinging plate at $x/D = 5$. In the radial direction (r), the grid spacing of $\Delta r/D = 0.01$ for the first 12 grid points are uniform close to the axis and then the grid spacing gradually decreases to $\Delta r/D = 0.001$ at $r/D = 0.5$ for *Block 1* and *Block 2*. For $0.5D < r \leq 3D$, the grid spacing is increased to $\Delta r/D = 0.02$ and maintained up to $r/D = 6.5$. Large vortical structures are then damped with a higher stretching ratio till $r/D = 12$. A grid sensitivity study was conducted

Block	x/D	r/D	$N_x \times N_r$	k_θ/N_θ	$\Delta x/D$	$\Delta r/D$
1	$[-0.04, 0]$	$[0, 0.5]$	40×84	$128/258$	0.001	$[0.01, 0.001]$
2	$[0, 5]$	$[0, 0.5]$	644×84	$128/258$	$[0.0002, 0.02]$	$[0.01, 0.001]$
3	$[0, 5]$	$[0.5, 0.6]$	644×69	$128/258$	$[0.0002, 0.02]$	$[0.001, 0.004]$
4	$[0, 5]$	$[0.6, 12]$	644×576	$128/258$	$[0.0002, 0.02]$	$[0.004, 0.08]$
5	$[0, 5]$	$[12, 30]$	644×90	$128/258$	$[0.0002, 0.02]$	$[0.08, 0.3641]$

Table 1. Summary for the size and the grid information of each block.

and the current grids were found to produce grid independent results. A zonal characteristic boundary condition [10] is then applied to avoid reflections of spurious acoustic waves in the *Block 5*. The azimuthal direction (θ) is resolved by 128 Fourier modes (k_θ), resulting in 258 collocation points (N_θ) for all the blocks. The size and number of points used for each block are summarised in table1. The jets are configured with an infinite lip, a nozzle pressure ratio ($NPR = P_{stag}/P_{air}$) of 3.4 and a distance (h) between the jet exit and the impinging plate is $5D$, where D is the nozzle exit diameter, P_{stag} and P_{air} are the stagnation pressure and the ambient pressure, respectively. The confined impinging jets are characterised with a Reynolds number ($Re_j = U_j D_j/\nu_{air}$) of 6×10^4, where D_j is the nozzle diameter of equivalent ideally expanded jets , U_j and ν_{air} are the ideally expanded jet velocity and the kinematic viscosity of the ambient air, respectively. The current jet parameters are chosen for comparison with previous experimental data [11] at the same working condition.

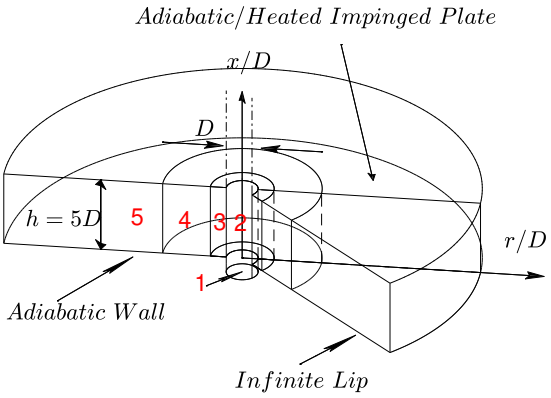

Figure 1. Schematic of the computational domain with 5 blocks.

Since strong shock waves exist for the current NPR, a shock sensor proposed by [4] is applied to the code. The sensor is implemented for its robustness in solving shock-turbulence interactions. Figure 2 shows the instantaneous snapshot of the non-dimensionalised density for the heated case overlaid with black dots representing the application of the shock sensor. It can be seen that most of the filtering points are located at the shock waves. Therefore the current filter does not affect the free shear layer and the impingement wall regions. This gives us confidence to investigate the heat transfer problem close to the impingement wall without the contamination of the shock filtering. It needs to be mentioned that the threshold for the shock filtering is dependent on the Reynolds number and the compressibility. For the current Reynolds number and NPR, the threshold was chosen to be 0.02 to ensure a stable solution.

Results

To validate the current data, figure 3 shows the comparison of the mean axial velocity between the adiabatic case and the experimental results from [11] at a Reynolds number around 10 times higher than the current simulation. Good agreements is

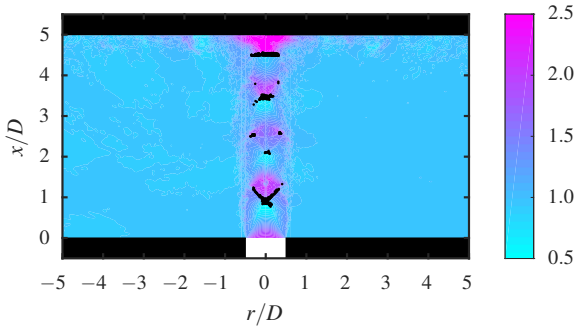

Figure 2. Snapshot of non-dimensionalised density field for the heated case. The color scale ranges from 0.5 to 2.5. The overlaid black dots indicate the locations where the shock sensor applied.

achieved, except that the location of the first shock wave for the current data is a bit upstream of that of [11]. A similar discrepancy was also observed by [12] and may be caused by the difference of Reynolds number or the LES sensitivity to the inlet condition.

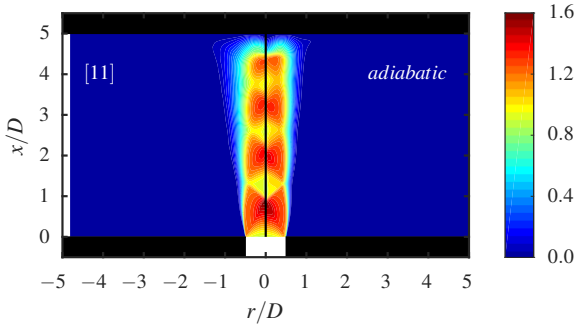

Figure 3. Comparison of the non-dimensionalised mean axial velocity between the experimental data [11] (left half) and the current adiabatic case (right half). The color scale ranges from 0 to 1.6.

To evaluate the contribution of the SGS modelling for the current LES, the ratio of the averaged subgrid scaled viscosity ($\overline{\mu_{sgs}}$) over the molecular viscosity ($\overline{\mu}$) is shown in figure **??**, where the left half figure is for the heated case and the right half figure is for the adiabatic case. The maximum values for both cases are expected to be located where strong shock waves occur in the main jet plumes. Values of the ratio are less than 1.1 in the shear layer and less than 0.7 in the wall jet at $r/D \leq 5$, respectively. Compared with the ratios from [2] ($\overline{\mu_{sgs}}/\overline{\mu} \simeq 10$ in the shear layer), the current two cases meet the requirement of LES and imply a higher resolution than used in [2].

To achieve a good prediction of heat transfer at the impingement plate, it is necessary to resolve the viscous sublayer. Figure 5(a) shows the dimensionless wall distance (x^+) on the impingement plate. It can be found that the maximum x^+ for the heated and adiabatic cases are respectively 0.81 and 1.15 at around $r/D = 0.56$. At $r/D = 1.43$, there is another small local peak for both

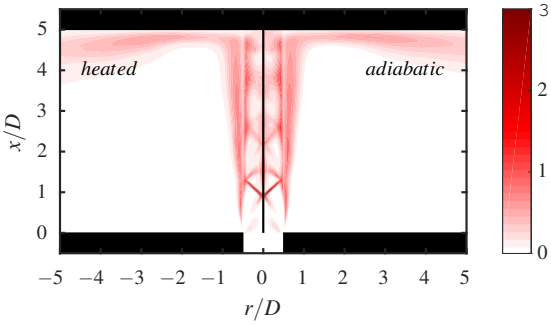

Figure 4. The ratio of the mean subgrid scaled viscosity $\overline{\mu_{sgs}}$ over the mean molecular viscosity $\overline{\mu}$ for the heated case (left half) and the adiabatic case (right half).

cases. Figure 5(b) shows the number of grid points close to the impingement plate along the radial direction. It can be seen that at least 6 points are within the sub-layer region, which ensures a good wall resolution to investigate the heat transfer for the current impingement jets.

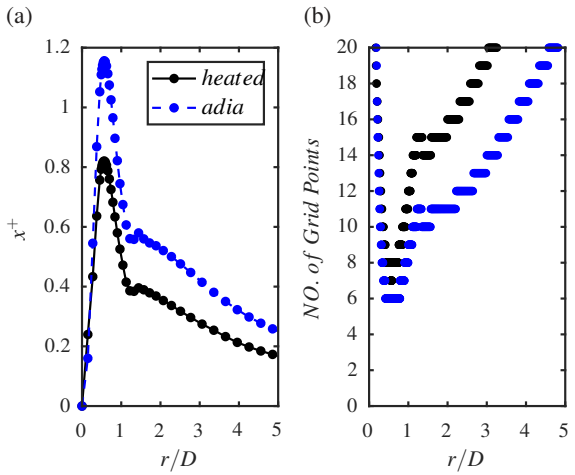

Figure 5. (a): dimensionless wall distance (x^+) normal to the impingement plate; (b): number of points within the viscous sub-layer ($x^+ \leq 5$) as a function of the radial distance along the impingement wall. Results of the heated/adiabatic cases are labelled with black/blue, respectively.

To quantify the convective heat transfer rate, the distribution of Nusselt number along the wall is usually used and is defined as,

$$Nu = \frac{D}{T_w - T_{ref}} \frac{\partial T}{\partial x}|_w. \quad (1)$$

where, T_w is the wall temperature, T_{ref} is the reference temperature. As it is suggested by multiple experiments such as [5], T_{ref} shall be equal to the adiabatic wall temperature since the cooling effects under the supersonic jet condition would cause strong non-uniform adiabatic wall temperatures. This is contrary to the subsonic jet condition resulting in a uniform adiabatic wall temperature. Besides, the shock waves in the jet plume would cause an energy loss and thus lead to an inaccurate prediction of heat transfer. Lastly, when using the adiabatic wall temperature as the reference temperature, the heat transfer coefficient is found to be independent of the temperature difference between the jet and the surroundings [13].

Figure 6(a) shows the Nusselt number distribution scaled by $Re^{0.52}$ along the wall. The scaling is chosen to allow us to compare our results with [5]. Figure 6(b) shows the maximum Nusselt numbers as a function of their radial locations

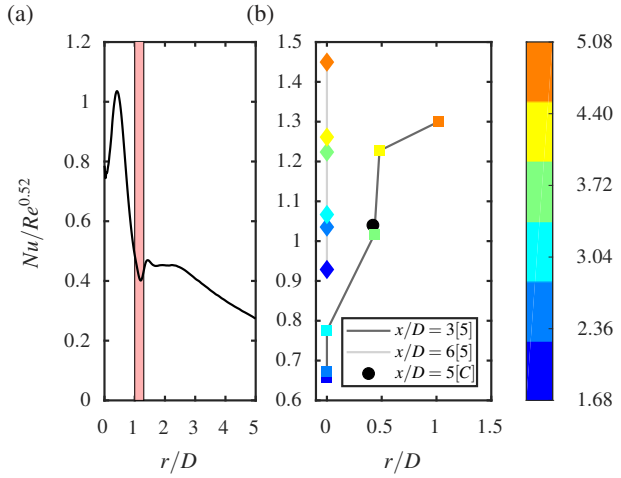

Figure 6. (a): Nusselt number distribution along the wall; (b): the maximum Nusselt numbers as a function of their radial locations from [5] for the jet-plate distance ratios (x/D) of 3 and 6 at six NPRs labelled with different colors. The current data is labelled with a black dot.

from [5] at the distance ratios (x/D) of 3 and 6, and the current data at $x/D = 5$. For $x/D = 6$, the maximum Nusselt numbers are consistently located at the stagnation point, irrespective of the values of NPR. However for $x/D = 3$, the maximum Nusselt numbers are shifted away from the stagnation point as the NPRs exceed 3.72. The current data provides a similar shifting phenomenon, which may imply a threshold of $x/D = 5$ for the jet-plate distance based on the current investigated cases. A secondary dip and peak are found at around $r/D = 1.2$ and $r/D = 1.43$ in figure 6(a). Similar observations were made by [5] with a shorter distance ratio and moderate NPRs. However to the authors' best knowledge, no solid reasons have been provided to explain this phenomenon for supersonic conditions.

A barycentric map which was proposed by [14] is presented in figure 7 to study the relatively dominant components of the anisotropy tensor. The findings are intended to offer a physical explanation for the secondary dip and peak in Nusselt numbers. A contoured color method [15] is applied to illustrate the map clearly. The current chosen color scheme is specifically localised to the corners of the map to emphasise the anisotropy close to the impingement wall. The three tips of the triangle in the anti-clockwise direction indicate one-component turbulence (1 *comp*), two-component axisymmetric turbulence (2 *comp*) and isotropic turbulence (3 *comp*) which are colored by red, green and blue, respectively. The intermediate colors represent two-component, axisymmetric contraction and axisymmetric expansion turbulence states with yellow, cyan and pink. Figure 8 shows the anisotropy map for the impingement region of the heated (a) and the adiabatic (b) case. It can be found that the turbulence anisotropy is similar for both cases. No isotropic turbulence can be found close to the wall. At $1.0 \leq r/D \leq 1.175$, two-component turbulence is found close to the plate with yellow followed by axisymmetric contraction turbulence colored from dark green to light green. Away from the plate, the flow is dominated by axisymmetric expansion, which is caused by the development of the wall jet. At $1.175 < r/D \leq 1.35$, the radial stress dominates but the axial and the azimuthal components are negligible. This resembles the movements of the shock waves in one single direction. Shocklets at similar radial locations were reported by an experimental study [3]. They would raise the local temperature and thus reduce the efficiency of the heat transfer. Downstream of the shocklets, the flow will accelerate again, leading to the reduction of the thickness of the thermal boundary layer and will thus raise the heat transfer rate.

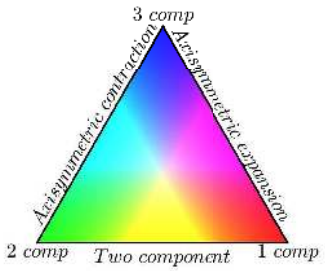

Figure 7. Barycentric map [14] overlaid with a vivid color contour [15] for the structure of turbulence anisotropy.

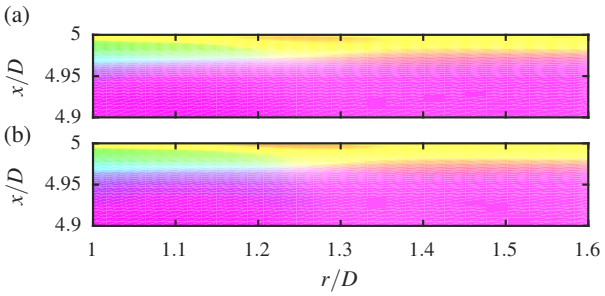

Figure 8. Presentation of the Reynolds stress anisotropy turbulence colored by [15] for the heated case (a) and the adiabatic case (b) close to the impingement wall.

Conclusions

The heat transfer of under-expanded supersonic impinging jets at a Reynolds number of 6×10^4, a distance ratio (h/D) of 5 and a nozzle pressure ratio (NPR) of 3.4 has been investigated using compressible-flow LES. A shock sensor was first implemented into the code for the flow fields with strong shock waves to enable a stable and accurate solution. To achieve a good LES resolution for the current study of heat transfer, the ratio of turbulent viscosity over the molecular viscosity is restricted to be less than 1.1, except for the locations of the shock waves. In addition, a very fine resolution close to the impingement wall was maintained. The current data showed good agreement with experimental results. The Nusselt number distribution was then presented and highlighted a shifted maximum, a second minimum and a second maximum value along the impingement wall. An anisotropy invariant map was further provided and illustrated a shocklet-resembling feature at the location where the second minimum Nusselt number occurs. The location of the shocklet is consistent with that observed in experimental data. It is proposed that the second minimum in Nusselt number is caused by the low heat removal capacity at the shocklet and the second maximum value is obtained by the strong advection behind the shocklet in the wall jet.

Acknowledgements

This work was supported by the financial support of the Australian Research Council and the resources were provided by the Pawsey Supercomputing Centre with funding from the Australian Government and the Government of Western Australia.

References

[1] Shukla, A. K. and Dewan, A. (2017). Flow and thermal characteristics of jet impingement: comprehensive review. *International Journal of Heat and Technology*, 35(1), 153–166 (DOI:10.18280/ijht.350121).

[2] Dauptain, A. and Cuenot, B. and Gicquel, L. Y. M. (2010). Large eddy simulation of stable supersonic jet impinging on flat plate. *AIAA journal*, 48(10), 2325–2338 (DOI:10.2514/1.J050362).

[3] Weightman, J. L. and Amili, O. and Honnery, D. and Soria, J. and Edgington-Mitchell, D. (2017). An explanation for the phase lag in supersonic jet impingement. *Journal of Fluid Mechanics*, 815, 421–448 (DOI:10.1017/jfm.2017.37).

[4] Uzun, A. and Kumar, R. and Hussaini, M. Y. and Alvi, F. S. (2013). Simulation of Tonal Noise Generation by Supersonic Impinging Jets. *AIAA journal*, 51(7), 1593–1611 (DOI:10.2514/1.J051839).

[5] Rahimi, M. and Owen, I. and Mistry, J. (2003). Impingement heat transfer in an under-expanded axisymmetric air jet. *International Journal of Heat and Mass Transfer*, 46(2), 263–272 (DOI:10.1016/S0017-9310(02)00275-2).

[6] Sandberg, R. D. (2015). Compressible-Flow DNS with Application to Airfoil Noise. *Flow, Turbulence and Combustion*, 95, 211–229 (DOI:10.1007/s10494-015-9617-1).

[7] Nicoud, F. and Ducros, F. (1999). Subgrid-scale stress modelling based on the square of the velocity gradient tensor. *Flow, Turbulence and Combustion*, 62(3), 183–200 (DOI:10.1023/A:1009995426001).

[8] Otero-Pérez, J. Javier and Sandberg, R. D. (2020). Compressibility and variable inertia effects on heat transfer in turbulent impinging jets. *Journal of Fluid Mechanics*, 887, A15. (DOI:10.1017/jfm.2020.5).

[9] Bodony, D. J. and Lele, S. K. (2005). On using large-eddy simulation for the prediction of noise from cold and heated turbulent jets. *Physics of Fluids*, 17(8), 1–20 (DOI:10.1063/1.2001689).

[10] Sandberg, R. D. and Sandham, N. D. (2006). Nonreflecting zonal characteristic boundary condition for direct numerical simulation of aerodynamic sound. *AIAA journal*, 44(2), 402–405 (DOI:10.2514/1.19169).

[11] Weightman, J. L. and Amili, O. and Honnery, D. and Edgington-Mitchell, D. and Soria, J. (2019). Nozzle external geometry as a boundary condition for the azimuthal mode selection in an impinging underexpanded jet. *Journal of Fluid Mechanics*, 862, 421–448 (DOI:10.1017/jfm.2018.957).

[12] Karami, S. and Edgington-Mitchell, D. and Soria, J. (2018). Large eddy simulation of supersonic underexpanded jets impinging on a flat plate. in *Proc. 11th Australasian Heat and Mass Transfer Conference*, RMIT University, Melbourne, Australia.

[13] Viskanta, R. (1993). Heat transfer to impinging isothermal gas and flame jets. *Experimental thermal and fluid science*, 6(2), 111–134 (DOI:10.1016/0894-1777(93)90022-B).

[14] Banerjee, S. and Krahl, R. and Durst, F. and Zenger, C. (2007). Presentation of anisotropy properties of turbulence, invariants versus eigenvalue approaches. *Journal of Turbulence*, 8(32), 1–28 (DOI:10.1080/14685240701506896).

[15] Emory, M. and Iaccarino, G. (2014). Visualizing turbulence anisotropy in the spatial domain with componentality contours. *Center for Turbulence Research Annual Research Briefs*, 123–138